ELSEVIER

A consistent dynamic localization model for large eddy simulation of turbulent flows based on a variational formulation

Volker Gravemeier *

Center for Turbulence Research, Stanford University, Stanford, CA 94305, USA

Abstract

In this study, a new approach for the dynamic localization model, which was originally proposed in Ghosal et al. [S. Ghosal, T.S. Lund, P. Moin, K. Akselvoll, A dynamic localization model for large-eddy simulation of turbulent flows, J. Fluid Mech. 286 (1995) 229–255], is described. This approach is integrated in a consistent manner into large eddy simulation based on a variational formulation. As a result, the variationally formulated condition for the model parameter is considered as an additional equation in a resulting system of two variational equations. This variational system may then be implemented using either a finite element or a finite volume method. The new version of the dynamic localization model proposed in this work has three advantages compared to the original dynamic localization model in Ghosal et al.: it relies on a simpler formulation overall, it obviates any iterative solution procedure, and it requires the solution of a number of small independent local equations instead of one large global equation. These three advantages make its solution theoretically easier and computationally more efficient. The new consistent dynamic localization model is tested for two different numerical flow examples, turbulent flow in a channel and turbulent flow in a planar asymmetric diffuser.
© 2006 Elsevier Inc. All rights reserved.

Keywords: Turbulence; Large eddy simulation; Variational formulation; Subgrid-scale modeling; Dynamic localization model

1. Introduction

The modeling of the unresolved or subgrid scales is a crucial aspect of large eddy simulation (LES) of turbulent flows. In the traditional LES, two different ways of subgrid-scale modeling may generally be distinguished according to [27]. One approach intends to approximate the subgrid-scale stress tensor τ itself. This strategy is called *structural modeling*. Another approach aims at modeling the (energetic) action of the unresolved (or subgrid) scales on the resolved scales rather than modeling the tensor itself. This second strategy is called *functional modeling*. A very popular form of functional modeling relies on the subgrid (or eddy) viscosity concept, which is based on the Boussinesq turbulent (or eddy) viscosity assumption. According to

* Present address: Chair for Computational Mechanics, Technical University of Munich, Boltzmannstr. 15, D-85747 Garching, Germany. Tel.: +49 89 28915245; fax: +49 89 28915301.
E-mail address: vgravem@lnm.mw.tum.de.

this concept, the deviatoric part of τ is approximated by a product of a subgrid viscosity v_T and the rate-of-strain tensor of the resolved scales.

The remaining unknown in this form of functional modeling is the subgrid viscosity v_T, and several approximations for v_T have been proposed in the meantime. The Smagorinsky [29] model was the first proposal in this context and is still a commonly used one due to its simplicity. However, that model is still based on an unknown parameter C_S. Choosing a constant value for this parameter over the entire domain has been proven to be an inadequate approach in most of the cases, although recent integrations of this simple constant-coefficient-based Smagorinsky model into a multiscale environment have revitalized it and yielded very good results for a number of test cases (see, e.g., [7,9,13,14,17]). Within the multiscale environment, the subgrid-scale model is directly applied only to the smaller resolved scales after a separation of the range of resolved scales. The reader may, for instance, consult the initial publication on the variational multiscale method for LES (i.e., [12]) for the basic idea. For a specific finite-volume or combined finite-element/finite-volume method within the variational multiscale LES, it is referred to [7,17], respectively. A comprehensive overview has recently been provided in [8], see also references therein for further elaboration.

An important improvement of the Smagorinsky model was introduced in [5], where the model parameter was determined as a function of position and time by way of a dynamic algorithm. It should be remarked that this dynamic procedure is not restricted to the Smagorinsky model as the underlying model, although it has mostly been used with that model. The original formulation of the dynamic algorithm in [5] contained a mathematically inconsistent assumption, which disregarded the fact that C_S is a rapidly varying function of position, as discussed in [22].

This inconsistency was later overcome in [6] by the introduction of the dynamic localization model. Furthermore, ad hoc schemes were addressed in this publication, which were usually applied in practical simulations to prevent them from becoming unstable. By using those ad hoc schemes, the application of the dynamic model in several problem configurations was enabled, without, however, being justified except in a heuristic way. Overall, the study in [6] aimed at "putting the dynamic modeling procedure on firm theoretical foundations, so that the method could be applied to arbitrary inhomogeneous flows without recourse to ad hoc procedures". After all, however, the actual way of calculating the model parameter based on a variationally formulated condition for C_S, which eventually had to make use of Fredholm's integral equation of the second kind for its solution, appeared to be rather complicated. Moreover, an iterative procedure was necessary to actually solve this integral equation in practical calculations, which made it a computationally expensive part of the overall simulation. This study was complemented by another study in [2], which addressed the issue of representing backscatter in the dynamic localization model by a stochastic modeling approach.

In an approximate version of the dynamic localization model proposed in [26], an iterative procedure was avoided by using an approximation in time, which, however, was accurate only up to the respective order of accuracy of the temporal approximation scheme. Moreover, this method faced, on the one hand, potential numerical instabilities and, on the other hand, potential inaccuracies in the case of rapid variations in the temporal evolution of the function, as admitted in [26]. However, the authors assumed the evolution of C_S to be a fairly slowly varying function of time due to the temporal filtering, which is implicitly introduced by the spatial filtering. Another recent approach in [31] makes the dynamic localization model less demanding by relying on an averaging procedure over homogeneous coordinate directions. However, this approach is not applicable to arbitrary inhomogeneous flows.

In the present study, LES is based on a variational formulation. In contrast to a traditional filter-based formulation, the resolution of the underlying numerical discretization is used to define the resolved part of the velocity u^h, with the superscript h indicating the characteristic length scale of the discretization. It should be remarked that this is actually a usual way of defining the resolved scales in practical LES, whenever the respective discretization is assumed to act as an implicit filter, and no further explicit filter is applied. The reason for introducing a subgrid-scale model in the variational formulation is mathematically different from the usual necessity of introducing a model term due to the appearance of a subgrid-scale stress tensor in the strong formulation of the Navier–Stokes equations in a traditional LES. Nevertheless, the physical necessity of accounting for the missing effect of unresolved scales on the resolved scales is the same in both cases. In order to account for this effect in the present study, it is resorted to the subgrid viscosity concept and, furthermore, the Smagorinsky model as one way of functional modeling, as mentioned above. Within a variational formu-

lation of the Navier–Stokes equations, the variationally formulated condition for C_S in the dynamic localization model according to [6] may easily be integrated to get a system of two variational equations. Hence, a consistent formulation in that both the underlying equation system (i.e., the incompressible Navier–Stokes equations) and the equation for C_S are in variational form is achieved.

A crucial ingredient of a dynamic modeling procedure is the separation of the resolved scales into large and small resolved scales. While this separation may easily be done in spectral space by using a sharp cutoff filter, discrete smooth filters are usually applied in physical space. However, scale-separating operators based on combined multigrid operators were recently proposed in [7] as an alternative way of separating the scales. A similar multigrid approach within a finite volume method was proposed in [30]. A mathematical analysis of multilevel approaches for the numerical simulation of turbulent flows can be found in [3]. It was shown in [7,9] that multigrid-based scale-separating operators, in particular one which provides a projective scale separation are superior in terms of quality of results and computational efficiency compared to discrete smooth filters. This projective operator, also serves as the basis for the version of the dynamic localization model to be developed in this work. This consistent dynamic localization model will also be tested in the context of the variational multiscale LES. As mentioned above, the separation of the resolved scales in the variational multiscale LES is not only needed for the calculation of the model parameter, but also for the identification of the smaller resolved scales, to which the subgrid-scale model is eventually applied. The scale-separating operators based on combined multigrid operators are well-suited to serve both these purposes, as already shown in [7,9] for a "standard" dynamic modeling procedure according to [5].

The final variational equation system may serve as the starting point for either a finite element or a finite volume formulation. A particular finite element method for variational multiscale LES may be found in [10], and the aspects of a finite volume formulation for variational multiscale LES were described in [7]. In this work, all theoretical developments will be done in a general manner, so that both finite element and finite volume implementations may easily be derived from it. The simulations at the end of this study have been conducted using the CDP-α code, the flagship LES code of the Center for Turbulence Research. Underlying this code is a finite volume method particularly suited for applications in complex geometries on unstructured grids.

The remainder of this paper is organized as follows. In Section 2, the basic and multiscale variational formulations are introduced, and the separation of scales using the projective scale-separating operator is outlined. Section 3 contains the dynamic modeling procedures, including a brief description of the original dynamic model with various ad hoc schemes and the development of the new approach for the dynamic localization model. The results for two numerical flow examples, turbulent flow in a channel and turbulent flow in a diffuser, are shown in Section 4. Within these applications, the consistent dynamic localization model is compared to the dynamic model with ad hoc schemes, which were previously used for the respective flow examples. In Section 5, conclusions are drawn from this study.

2. Variational formulations and separation of scales

2.1. Basic and multiscale variational formulation of the incompressible Navier–Stokes equations

The set of incompressible Navier–Stokes equations is given as

$$\frac{\partial \boldsymbol{u}}{\partial t} + \nabla \cdot (\boldsymbol{u} \otimes \boldsymbol{u}) + \nabla p - 2v\nabla \cdot \boldsymbol{\varepsilon}(\boldsymbol{u}) = \boldsymbol{f} \quad \text{in } \Omega \times (0, T), \tag{1}$$

$$\nabla \cdot \boldsymbol{u} = 0 \quad \text{in } \Omega \times (0, T), \tag{2}$$

where $\boldsymbol{u}$ denotes the velocity vector, p the kinematic pressure (i.e., pressure divided by density), v the kinematic viscosity, $\boldsymbol{f}$ the body force vector, Ω the domain of the problem, and T the simulation time. An initial condition

$$\boldsymbol{u} = \boldsymbol{u}_0 \quad \text{in } \Omega \times \{0\}, \tag{3}$$

where the initial velocity field $\boldsymbol{u}_0$ is assumed to be divergence-free, is also given. Furthermore, a Dirichlet boundary condition

$$\boldsymbol{u} = \boldsymbol{g} \quad \text{on } \Gamma_g \times (0, T) \tag{4}$$

is prescribed on the respective subset Γ_g of the domain boundary Γ.

A variational form of the Navier–Stokes equations may be achieved by starting with a weighted residual formulation as

$$\boldsymbol{B}_{\mathrm{NS}}(\boldsymbol{v},q;\boldsymbol{u},p) = (\boldsymbol{v},\boldsymbol{f})_{\Omega} \quad \forall\{\boldsymbol{v},q\} \in \mathscr{V}_{\boldsymbol{up}}, \tag{5}$$

where $\mathscr{V}_{\boldsymbol{up}}$ denotes the combined form of the weighting function spaces for velocity and pressure in the sense that $\mathscr{V}_{\boldsymbol{up}} := \mathscr{V}_{\boldsymbol{u}} \times \mathscr{V}_{p}$. The form $B_{\mathrm{NS}}(\boldsymbol{v},q;\boldsymbol{u},p)$ on the left hand side is hereby defined as

$$\boldsymbol{B}_{\mathrm{NS}}(\boldsymbol{v},q;\boldsymbol{u},p) = \int_{\Omega} \boldsymbol{v}\frac{\partial \boldsymbol{u}}{\partial t}\mathrm{d}\Omega + \int_{\Omega} \boldsymbol{v}\nabla \cdot (\boldsymbol{u} \otimes \boldsymbol{u})\mathrm{d}\Omega + \int_{\Omega} \boldsymbol{v}\nabla p\,\mathrm{d}\Omega - \int_{\Omega} \boldsymbol{v}2v\nabla \cdot \boldsymbol{\varepsilon}(\boldsymbol{u})\mathrm{d}\Omega - \int_{\Omega} q\nabla \cdot \boldsymbol{u}\,\mathrm{d}\Omega, \tag{6}$$

with $\boldsymbol{v}$ and q denoting the weighting functions. The L_2-inner product in the domain Ω on the right hand side is defined as usual:

$$(\boldsymbol{v},\boldsymbol{f})_{\Omega} = \int_{\Omega} \boldsymbol{v}\boldsymbol{f}\ \mathrm{d}\Omega. \tag{7}$$

The weighted residual formulation defined in (5)–(7) may serve as the starting point for either a finite element or a finite volume formulation. A more detailed discussion of the finite element formulation can be found, for instance, in [10]. The corresponding development for a finite volume formulation is provided in [7].

In either case, the prerequisite for the application of the respective method is a discretization of the domain Ω into n elements or control volumes Ω_i $(i = 1, \ldots, n)$ with element or control volume boundaries Γ_i, respectively. In the following, it will be referred to Ω_i as an "element" for brevity, which is, however, assumed to be replaced by the notation "control volume" in the context of the finite volume method. With h denoting the characteristic length scale of the discretization, the variational formulation for the discrete weighting and solution functions reads as

$$\boldsymbol{B}_{\mathrm{NS}}(\boldsymbol{v}^h,q^h;\boldsymbol{u}^h,p^h) = (\boldsymbol{v}^h,\boldsymbol{f})_{\Omega} \quad \forall\{\boldsymbol{v}^h,q^h\} \in \mathscr{V}_{\boldsymbol{up}}^h, \tag{8}$$

where $\mathscr{V}_{\boldsymbol{up}}^h$ indicates the discrete weighting function space, and the appropriate integration-by-parts procedures have to be implemented for either the finite element or the finite volume method, see [10] or [7], respectively. In LES, the characteristic length scale h is usually considerably larger than the order of the smallest length scale of the problem. Thus, a large number of scales cannot be explicitly resolved. Therefore, the subgrid viscosity approach as a way of taking into account the (dissipative) effect of the unresolved scales is applied. According to this, a subgrid viscosity term in weighted formulation is added to (8), resulting in

$$\boldsymbol{B}_{\mathrm{NS}}(\boldsymbol{v}^h,q^h;\boldsymbol{u}^h,p^h) - (\boldsymbol{v}^h, \nabla \cdot (2v_{\mathrm{T}}\boldsymbol{\varepsilon}(\boldsymbol{u}^h)))_{\Omega} = (\boldsymbol{v}^h,\boldsymbol{f})_{\Omega} \quad \forall\{\boldsymbol{v}^h,q^h\} \in \mathscr{V}_{\boldsymbol{up}}^h, \tag{9}$$

where v_{T} denotes the subgrid viscosity. The weighted subgrid viscosity term in (9) is also given without any integration-by-parts procedure, in order to keep the notation open for the application of the respective numerical method, which results in a variationally formulated subgrid viscosity term eventually.

An alternative approach is LES based on the variational multiscale method, where the weighted subgrid viscosity term is only added to the smaller scales of the resolved scale range as

$$\boldsymbol{B}_{\mathrm{NS}}(\boldsymbol{v}^h,q^h;\boldsymbol{u}^h,p^h) - (\boldsymbol{v}'^h, \nabla \cdot (2v_{\mathrm{T}}'\boldsymbol{\varepsilon}(\boldsymbol{u}'^h)))_{\Omega} = (\boldsymbol{v}^h,\boldsymbol{f})_{\Omega} \quad \forall\{\boldsymbol{v}^h,q^h\} \in \mathscr{V}_{\boldsymbol{up}}^h, \boldsymbol{v}'^h \in \mathscr{V}_{\boldsymbol{up}}'^h, \tag{10}$$

where $\boldsymbol{v}'^h$ and $\boldsymbol{u}'^h$ denote the small-scale part of the velocity weighting and solution function, respectively. In (10), the subgrid viscosity term with the subgrid viscosity v_{T}' directly acts only on the small resolved scales. Indirect influence on the large resolved scales, however, is ensured due to the coupling of the large and the small resolved scales (see, e.g., [7] for details).

The goal of this work is to find appropriate modeling approaches for the subgrid viscosity v_{T} and v_{T}', respectively, in the context of a variational formulation. Before turning to this issue, effective ways to separate the resolved scales of the problem (i.e., to differentiate the larger and the smaller resolved scales) are required to be established. For the multiscale formulation (10), the necessity for the separation is already obvious in the formulation itself. However, irrespective of the range of resolved scales, which the subgrid viscosity is added to (i.e. the complete range in (9) or the range of smaller scales in (10)), any dynamic modeling procedure according to [5] requires such a separation of scales, as will be shown below.

2.2. Projective scale separation

The scale separation used in this work relies on combined multigrid operators, and it was originally presented in [7]. It refers to the level of complete resolution indicated by the characteristic length h and identifies *a priori* a large-scale resolution level with respect to this complete resolution level characterized by the length $\bar{h}$, where $\bar{h} > h$. As a result, a large-scale part of the velocity $\bar{\boldsymbol{u}}^h$ on the large-scale resolution level is extracted. The small-scale part of the velocity is defined on the level of complete resolution, which is characterized by the length h, as

$$\boldsymbol{u}'^h = \boldsymbol{u}^h - \bar{\boldsymbol{u}}^h, \tag{11}$$

where $\bar{\boldsymbol{u}}^h$ is the large-scale value transferred to this level. In practice, two grids are created: a coarser grid, which is called the "parent" grid, and a finer grid, which is called the "child" grid. The child grid is obtained by an isotropic hierarchical subdivision of the parent grid. More details concerning the implementation can be found in [7].

The general class of scale-separating operators based on multigrid operators is formulated as

$$\bar{\boldsymbol{u}}^h = S^{\mathrm{m}}[\boldsymbol{u}^h] = P \circ R[\boldsymbol{u}^h] = P[\bar{\boldsymbol{u}}^{\bar{h}}], \tag{12}$$

where the scale-separating operator S^{m} consists of the sequential application of a restriction operator R and a prolongation operator P. Applying the restriction operator on $\boldsymbol{u}^h$ yields a large-scale velocity $\bar{\boldsymbol{u}}^{\bar{h}}$ defined at the degrees of freedom of the parent grid, which is then prolongated, in order to obtain a large-scale velocity $\bar{\boldsymbol{u}}^h$ defined at the degrees of freedom of the child grid. Various restriction as well as prolongation operators may be used in (12). Two special combinations of restriction and prolongation operators were analyzed and used in [7,9]. Both of them rely on the same restriction operator, but apply different prolongation operators afterwards. The restriction operator R is defined to be a volume-weighted average over all the child elements within one parent element subject to

$$\bar{\boldsymbol{u}}_j^{\bar{h}} = \frac{\sum_{i=1}^{n_{\mathrm{cop}}} |\Omega_i| \boldsymbol{u}_i^h}{\sum_{i=1}^{n_{\mathrm{cop}}} |\Omega_i|}, \tag{13}$$

where $\bar{\boldsymbol{u}}_j^{\bar{h}}$ denotes the large-scale velocity at the center of the parent element $\bar{\Omega}_j$ and $\boldsymbol{n}_{\mathrm{cop}}$ the number of child elements in $\bar{\Omega}_j$. It was proven in [7] that only one of the two applied prolongation operators leads to a projective operator overall. The prolongation operator P^{p} yields a constant prolongation as

$$\bar{\boldsymbol{u}}_i^h = P^{\mathrm{p}}\left[\bar{\boldsymbol{u}}_j^{\bar{h}}\right]_i = \bar{\boldsymbol{u}}_j^{\bar{h}} \quad \forall \Omega_i \subset \bar{\Omega}_j \tag{14}$$

and zero elsewhere. The complete scale-separating operator is defined as

$$S^{\mathrm{pm}} := P^{\mathrm{p}} \circ R. \tag{15}$$

The property of a projector is indicated by the additional superscript "p".

3. Dynamic modeling procedures

All dynamic modeling procedures to be presented below use the Smagorinsky model [29] as its underlying model formulation. Thus, the subgrid viscosity is given as

$$v_{\mathrm{T}} = (C_{\mathrm{S}} h)^2 |\varepsilon(\boldsymbol{u}^h)|, \tag{16}$$

where $\varepsilon(\boldsymbol{u}^h)$ denotes the rate-of-strain tensor of the resolved scales. In the multiscale case, the dependence is restricted to the small scales as

$$v'_{\mathrm{T}} = (C_{\mathrm{S}} h)^2 |\varepsilon(\boldsymbol{u}'^h)| = (C_{\mathrm{S}} h)^2 |\varepsilon(\boldsymbol{u}^h - \bar{\boldsymbol{u}}^h)|. \tag{17}$$

The dynamic modeling procedure originally proposed in [5] relies on the Germano identity, see also [4]. This identity refers to a pointwise formulation of the Navier–Stokes equations for the discretized variables $\boldsymbol{u}^h$ and p^h, which already contains a subgrid-scale stress tensor to account for the scales still unresolved by this discretization. Hence, the momentum equation may be given as

$$\frac{\partial \boldsymbol{u}^h}{\partial t} + \nabla \cdot (\boldsymbol{u}^h \otimes \boldsymbol{u}^h) + \nabla p^h - 2\nu \nabla \cdot \boldsymbol{\varepsilon}(\boldsymbol{u}^h) + \nabla \cdot \boldsymbol{\tau}^h = \boldsymbol{f}^h, \tag{18}$$

where the only term added to a straightforward discretization of (1), the subgrid-scale stress tensor, is defined as

$$\boldsymbol{\tau}^h = (\boldsymbol{u} \otimes \boldsymbol{u})^h - \boldsymbol{u}^h \otimes \boldsymbol{u}^h. \tag{19}$$

Note that in (18) and (19) the usual filtered formulation is replaced by the actual implicit scale separation based on the chosen discretization with characteristic length scale h. The "test filter" is replaced by the scale-separating operator S^{pm}. Thus, the analog of the "subtest"-scale stress tensor can be expressed as

$$\bar{\boldsymbol{\tau}}^h = S^{\mathrm{pm}}[(\boldsymbol{u} \otimes \boldsymbol{u})^h] - S^{\mathrm{pm}}[\boldsymbol{u}^h] \otimes S^{\mathrm{pm}}[\boldsymbol{u}^h]. \tag{20}$$

Following this approach yields a value for the parameter C_S of the Smagorinsky model at every degree of freedom of the child grid. However, it was shown in [7] that the application of the scale-separating operators based on combined multigrid operators opens up the opportunity to determine the values only at the degrees of freedom of the parent grid. This is achieved by using the restriction operator R exclusively. In this work, the focus is on the formulation (20), where the complete scale-separating operator S^{pm} is applied.

3.1. Dynamic model using various ad hoc schemes

The Germano identity states the following:

$$\boldsymbol{L}^h = \bar{\boldsymbol{\tau}}^h - S^{\mathrm{pm}}[\boldsymbol{\tau}^h], \tag{21}$$

where $\boldsymbol{L}^h$ can be obtained as

$$\boldsymbol{L}^h = S^{\mathrm{pm}}[\boldsymbol{u}^h \otimes \boldsymbol{u}^h] - S^{\mathrm{pm}}[\boldsymbol{u}^h] \otimes S^{\mathrm{pm}}[\boldsymbol{u}^h] \tag{22}$$

by inserting (19) and (20) into (21).

Assuming the Smagorinsky model as an appropriate modeling term at both discretization levels and accounting for the fact that the Smagorinsky model is basically a "trace-free" model in the context of incompressible flow, Eq. (21) is modeled as follows:

$$\operatorname{dev}\boldsymbol{L}^h = \boldsymbol{L}^h - \frac{1}{3}\operatorname{tr}\boldsymbol{L}^h\boldsymbol{I} \approx -2(C_S\bar{h})^2|S^{\mathrm{pm}}[\boldsymbol{\varepsilon}(\boldsymbol{u}^h)]|S^{\mathrm{pm}}[\boldsymbol{\varepsilon}(\boldsymbol{u}^h)] + S^{\mathrm{pm}}\left[2(C_Sh)^2|\boldsymbol{\varepsilon}(\boldsymbol{u}^h)|\boldsymbol{\varepsilon}(\boldsymbol{u}^h)\right], \tag{23}$$

where $\boldsymbol{I}$ denotes the identity tensor, and modeling is obviously confined to the deviatoric part of the tensor $\boldsymbol{L}^h$. It is now assumed that C_S is constant over one element of the parent grid. Hence, Eq. (23) may be rewritten as

$$\operatorname{dev}\boldsymbol{L}^h \approx C_S^h\left(2S^{\mathrm{pm}}[|\boldsymbol{\varepsilon}(\boldsymbol{u}^h)|\boldsymbol{\varepsilon}(\boldsymbol{u}^h)] - 2\left(\frac{\bar{h}}{h}\right)^2|S^{\mathrm{pm}}[\boldsymbol{\varepsilon}(\boldsymbol{u}^h)]|S^{\mathrm{pm}}[\boldsymbol{\varepsilon}(\boldsymbol{u}^h)]\right) = C_S^h\boldsymbol{M}^h, \tag{24}$$

where the parameter expression $(C_Sh)^2$ is denoted by C_S^h here and below. This assumption neglects the important observation that C_S is a rapidly varying function of position, see [22]. This observation gave rise to the development of the dynamic localization model in [6]. However, following this assumption enables the calculation of the parameter expression C_S^h on the right hand side of (24) as a minimization of the error tensor

$$\boldsymbol{E}^h = \operatorname{dev}\boldsymbol{L}^h - C_S^h\boldsymbol{M}^h. \tag{25}$$

For this purpose, the least-squares approach proposed by [19] aims at fulfilling the minimization condition

$$\frac{\partial(\boldsymbol{E}^h\boldsymbol{E}^h)}{\partial C_S^h} = 2C_S^h\boldsymbol{M}^h\boldsymbol{M}^h - 2\operatorname{dev}\boldsymbol{L}^h\boldsymbol{M}^h = 0, \tag{26}$$

which, finally, leads to a formula for C_S^h as

$$C_S^h = \frac{\operatorname{dev}\boldsymbol{L}^h\boldsymbol{M}^h}{\boldsymbol{M}^h\boldsymbol{M}^h}. \tag{27}$$

Potential numerical problems may have to be faced related to either unbounded or negative (and, thus, anti-dissipative) values of C_S^h jeopardizing the stability of the simulation. Various ad hoc schemes have been used to avoid this potential instability. In a channel, the first numerical example of this work, both numerator and denominator in (27) are usually averaged over the homogeneous planes, exploiting the homogeneity of the flow in two coordinate directions. Additionally, clipping may be performed (i.e., potential negative values of C_S^h (and, hence, C_S) are set to zero artificially) subject to

$$C_S^h = \frac{1}{2}(C_S^h + |C_S^h|).$$ (28)

The dynamic model with averaging and clipping will be abbreviated DAMC (Dynamic Averaged Model with Clipping) in the context of the turbulent flow simulations in a channel in Section 4.

In the second numerical example of this work, a planar asymmetric diffuser, only one homogeneous direction exists. Of course, it may still be averaged over the remaining homogeneous direction. This approach with additional clipping in the sense of (28) was used for the second numerical example in [6], turbulent flow over a backward-facing step, which also exhibits one homogenous direction. It is, however, unquestionable that such an approach is inapplicable for all flow problems exhibiting no homogeneous direction at all.

One alternative for completely inhomogeneous flows is a procedure of local "smoothing" by averaging over neighbouring grid cells. This strategy was proposed and applied to turbulent flow in a lid-driven cavity in [33]. Additionally, a slightly different clipping was performed, in order to ensure that the total viscosity remains positive. Another alternative is the special clipping procedure proposed in [20] without any averaging or local smoothing. Here, the same values for C_S as above are used as long as C_S remains positive. As soon as C_S becomes negative, a different strategy is pursued. The parameter expression C_S^h is then calculated using

$$C_S^h = \sqrt{\frac{\operatorname{dev} \boldsymbol{L}^h \operatorname{dev} \boldsymbol{L}^h}{\boldsymbol{M}^h \boldsymbol{M}^h}}$$ (29)

instead of (27). Obviously, using (29) ensures a positive value for C_S^h and, hence, for C_S. The idea leading to (29) formulates the modeling relation as

$$\operatorname{dev} \boldsymbol{L}^h = C_S^h \boldsymbol{M}^h.$$ (30)

Contracting with itself both the left and the right hand side as

$$\operatorname{dev} \boldsymbol{L}^h \operatorname{dev} \boldsymbol{L}^h = (C_S^h)^2 \boldsymbol{M}^h \boldsymbol{M}^h$$ (31)

finally leads to (29). The dynamic model with the special clipping procedure using (29) will be abbreviated DMSC (Dynamic Model with Special Clipping) in the context of the simulations in Section 4. As already declared in [6], all of the aforementioned ad hoc schemes cannot be justified except in a heuristic way.

3.2. Dynamic localization model

The dynamic localization model is also based on the Germano identity (i.e., Eqs. (21)–(23) are still valid). However, the parameter expression C_S^h is not taken out of the scale-separating operation and, thus, the related mathematical inconsistency is taken back. As a result, the error tensor is rewritten as

$$\boldsymbol{E}^h = \operatorname{dev} \boldsymbol{L}^h - C_S^h \boldsymbol{A}^h + S^{\mathrm{pm}}[C_S^h \boldsymbol{B}^h],$$ (32)

where

$$\boldsymbol{A}^h = -2\left(\frac{\bar{h}}{h}\right)^2 |S^{\mathrm{pm}}[\boldsymbol{\varepsilon}(\boldsymbol{u}^h)]| S^{\mathrm{pm}}[\boldsymbol{\varepsilon}(\boldsymbol{u}^h)]$$ (33)

and

$$\boldsymbol{B}^h = -2|\boldsymbol{\varepsilon}(\boldsymbol{u}^h)|\boldsymbol{\varepsilon}(\boldsymbol{u}^h).$$ (34)

The scale-separating operator S^{pm} in (32) raises the dependency of the value for C_S^h in one child element to all other child elements within the same parent element. Using, for example, the alternative scale-separating operator S^{sm} proposed in [7] would extend the dependency by including child elements in neighbouring parent elements. Due to the extended dependency, a minimization procedure restricted to one point as expressed in (26) is no longer possible. Thus, the functional

$$\mathscr{F}[C_S^h] = \int_\Omega \boldsymbol{E}^h \boldsymbol{E}^h \mathrm{d}\Omega \tag{35}$$

was chosen in [6] to enforce a minimization in an integral sense over the entire domain Ω. Setting the variation of $\mathscr{F}$ to zero results in

$$\delta\mathscr{F}[C_S^h] = 2 \int_\Omega \delta\boldsymbol{E}^h \boldsymbol{E}^h \mathrm{d}\Omega = 0. \tag{36}$$

In [6], a strong solution of the corresponding Euler–Lagrange equation was searched. This led to a rather complicated equation for C_S^h in form of Fredholm's integral equation of the second kind, which was solved in an iterative procedure. All of this is not necessary here. Instead, this work proposes that Eq. (36) be considered as another variational equation to be solved in addition to the basic variational Eqs. (9) or (10), respectively. Thus, a system of two variational equations is established.

Remark. The solution of (36) may follow the so-called "variational principle", a concept well-known in the context of the finite element method. The reader may consult a standard textbook on the finite element method, such as [34], for elaboration. The variational principle specifies a functional depending in an integral form on an unknown function, which is here represented by the functional $\mathscr{F}$ and the unknown function $C_S^h(\boldsymbol{x}, t)$. The solution for the problem is a function C_S^h which makes $\mathscr{F}$ stationary with respect to small changes δC_S^h. For this purpose, the variation $\delta\mathscr{F}$ is set to zero, as shown in (36). The small change δC_S^h is implicitly contained in the small change δE^h in the error tensor function E^h in (36) and will be revealed below. As aforementioned, the variational principle is well-established in the finite element method, but only for problems, for which such a functional can be found. This requirement excludes a multitude of mechanical problems, among others, the present Navier–Stokes problem. Thus, the Navier–Stokes equations have been introduced into a weighted residual formulation above, which is the alternative and more general concept within the finite element method. However, both concepts, the weighted residual formulation and the variational principle, eventually lead to a variational formulation in the finite element method.

The problem is that, in general, the variational principle is not an appropriate concept in the finite volume method, which is intended to be applied in the numerical simulations below. In general, finite volume methods may be thought as Petrov–Galerkin methods, where the weighting function is a constant over the control volume. Under the particular circumstances of this relatively simple case (i.e., no derivatives of C_S^h contained in the error tensor function (32)), however, a similar solution approach for (36) may also be pursued with the finite volume method. Inserting (32) into (36) yields

$$2 \int_\Omega (-\delta C_S^h \boldsymbol{A}^h + S^{\mathrm{pm}}[\delta C_S^h \boldsymbol{B}^h])(\mathrm{dev}\,\boldsymbol{L}^h - C_S^h \boldsymbol{A}^h + S^{\mathrm{pm}}[C_S^h \boldsymbol{B}^h])\mathrm{d}\Omega = 0, \tag{37}$$

which can be rearranged as

$$\int_\Omega \delta C_S^h \boldsymbol{A}^h C_S^h \boldsymbol{A}^h \mathrm{d}\Omega - \int_\Omega \delta C_S^h \boldsymbol{A}^h S^{\mathrm{pm}}[C_S^h \boldsymbol{B}^h]\mathrm{d}\Omega - \int_\Omega S^{\mathrm{pm}}[\delta C_S^h \boldsymbol{B}^h]C_S^h \boldsymbol{A}^h \mathrm{d}\Omega + \int_\Omega S^{\mathrm{pm}}[\delta C_S^h \boldsymbol{B}^h]S^{\mathrm{pm}}[C_S^h \boldsymbol{B}^h]\mathrm{d}\Omega$$

$$= \int_\Omega \delta C_S^h \boldsymbol{A}^h \mathrm{dev}\,\boldsymbol{L}^h \mathrm{d}\Omega - \int_\Omega S^{\mathrm{pm}}[\delta C_S^h \boldsymbol{B}^h]\mathrm{dev}\,\boldsymbol{L}^h \mathrm{d}\Omega. \tag{38}$$

The first line of (38) contains the terms including the non-projected weighting function δC_S^h and the projected weighting function δC_S^h, respectively, and the second line the known terms depending on the deviatoric part of the tensor $\boldsymbol{L}^h$, weighted either by the non-projected or by the projected weighting function δC_S^h.

Note that (38) does not contain any derivatives of the function C_S^h. Thus, a third crucial advantage of the present approach with respect to [6], besides the advantages of a simpler formulation and no need for an iterative solution approach, can be attributed to the fact that (38) does not need to be solved as a global equation over the entire domain. It may rather be solved as a number of substantially smaller local equations, since the coupling of the values due to S^{pm} exists only within the range of each parent element. Thus, a sample equation defined in the parent element $\bar{\Omega}_j$ is given as

$$\sum_{i=1}^{n_{cop}} \int_{\Omega_i} \delta C_S^h \boldsymbol{A}^h C_S^h \boldsymbol{A}^h \mathrm{d}\Omega - \sum_{i=1}^{n_{cop}} \int_{\Omega_i} \delta C_S^h \boldsymbol{A}^h S^{pm}[C_S^h \boldsymbol{B}^h] \mathrm{d}\Omega - \sum_{i=1}^{n_{cop}} \int_{\Omega_i} S^{pm}[\delta C_S^h \boldsymbol{B}^h] C_S^h \boldsymbol{A}^h \mathrm{d}\Omega$$

$$+ \sum_{i=1}^{n_{cop}} \int_{\Omega_i} S^{pm}[\delta C_S^h \boldsymbol{B}^h] S^{pm}[C_S^h \boldsymbol{B}^h] \mathrm{d}\Omega = \sum_{i=1}^{n_{cop}} \int_{\Omega_i} \delta C_S^h \boldsymbol{A}^h \mathrm{dev}\, \boldsymbol{L}^h \mathrm{d}\Omega - \sum_{i=1}^{n_{cop}} \int_{\Omega_i} S^{pm}[\delta C_S^h \boldsymbol{B}^h] \mathrm{dev}\, \boldsymbol{L}^h \mathrm{d}\Omega, \qquad (39)$$

where, again, n_{cop} denotes the number of child elements Ω_i in $\bar{\Omega}_j$. All equations of type (39) can be solved independently. Thus, they are parallel to full extent in a multi-processor calculation, giving rise to substantial computational savings.

In Eq. (38), one has to deal exclusively with volume integrals. These may likewise be defined over element domains in a finite element method or over control volume domains in a finite volume method. The simplest approximation is chosen here by using discontinuous ansatz functions for the weighting and solution functions in a finite element method as well as for the solution function in a finite volume method. The weighting function in a finite volume method is already defined to be constant a priori (i.e., $\delta C_S^h = 1$ for the present case). In the end, one equation of type (39) has to be solved in each parent element. Thus, the overall number of equations which have to be solved is equal to the number of parent elements in the domain. The matrices resulting from each of these equations are of size $n_{cop} \times n_{cop}$. Usually (i.e., for hexahedral and tetrahedral elements), these amount to be 8×8 matrices. In the numerical simulations below, a direct solver, which is contained in the LAPACK solver package for dense linear systems, is used for the solution of these relatively small matrices.

Although the mathematical inconsistency is adequately addressed by this approach, the problem of obtaining potentially negative values for C_S^h and, hence, for C_S still exists. In [6], the constraint $C_S \geqslant 0$ was directly imposed. Analogous to this, clipping in the sense of (28) is also enforced for the numerical simulations of this work. Thus, the present approach resembles the dynamic localization model (constrained) in [6]. It will be abbreviated DLMC in Section 4.

Remark. An alternative model, which is called the dynamic localization model (k-equation), was also proposed in [6]. The crucial feature of this model is that it allows for backscatter of energy (i.e., C_S is allowed to take negative values). The sub grid-scale kinetic energy k is monitored, though, in order to rule out unphysical negative values. The drawback of this model is the enormous effort linked with it. Since the sub grid-scale kinetic energy appears in the model formulation, a global transport equation must be solved for k. The present approach is basically open to this. In this case, the already existing system of two variational equations would be extended by an additional global scalar equation, which might be solved as a variational equation, too. Furthermore, two equations would have to be solved for two parameters appearing in the transport equation for k. These equations are similar in their structure to the one which has to be solved for C_S^h (i.e., they may also be dealt with as a number of local equations). Thus, the dynamic localization model (k-equation) in the context of the present approach would require the solution of one additional global equation and two additional local equation systems.

4. Numerical examples

All numerical simulations in this section are conducted using the CDP-α code, an unstructured finite-volume-based CFD code designed for LES of variable density low Mach-number flows on very large grids using massively parallel computers (see, e.g., [11] and references therein). The main features are the use of a fractional-step procedure and a momentum interpolation method for unstructured grids. The Crank–Nicolson scheme, a fully implicit time-stepping scheme of second-order accuracy, is applied to the convective and viscous

terms, and, furthermore, the non-linear convective term is linearized about the result of the previous time step. All spatial and temporal approximations are of second-order accuracy. Furthermore, discrete conservation of energy is enforced. See [21] for this important aspect of the code. The matrix resulting from the momentum equation is solved using a simple iterative SOR procedure. For the solution of the pressure Poisson equation, an algebraic multigrid solver is used. See [11] for the details as well as some investigations concerning the performance of this multigrid solver. For comparison, simulations using no model at all (NM) are performed for both numerical examples. The multiscale simulations are indicated by adding "-MS" to the respective method abbreviation.

4.1. Turbulent channel flow

The numerical setup for turbulent flow in a channel is basically identical to that described in [7]. Flows at two different Reynolds numbers, $Re_\tau = u_\tau \delta_c / v = 180$ and $Re_\tau = 590$, are simulated marking the lower and upper end of the study in [24]. u_τ and δ_c denote the turbulent wall-shear velocity and the channel half-width, respectively. The channel dimensions are chosen according to [24] for the two cases. A parabolic velocity profile perturbed by a random velocity fluctuation of 10%-amplitude of the bulk mean streamwise velocity represents the initial condition u_0 for the velocity field, see [7] for details. No-slip boundary conditions are applied at the upper and lower wall in x_2-direction. In x_1- as well as x_3-direction, periodic boundary conditions for the velocity are applied. As the driving mechanism for the flow, a body force is imposed in form of a driving pressure gradient in the streamwise x_1-direction. The respective time step value for the temporal discretization is evaluated based on a fixed choice of the CFL number. The CFL number is hereby calculated according to the definition in [16]. For both Reynolds numbers, the CFL number is prescribed to be 0.65. 5000 time steps are performed to allow the flow to develop, and the statistics are collected during another 5000 time steps.

In the first part of the channel flow study, the spatial discretization for the lower Reynolds number case employs 32 control volumes in each coordinate direction. For the higher Reynolds number case, a discretization with 64 control volumes in each coordinate direction is employed. The distribution of control volumes in the wall-normal x_2-direction obeys a cosine function refining towards the walls for the parent grid, with the subsequent isotropic hierarchical subdivision procedure applied. In the second part, a grid refinement study for the higher Reynolds number case is conducted using the grid with 32 control volumes in each coordinate direction also for this case. Furthermore, grids employing 48 and 80 control volumes, respectively, are applied. Based on the findings in [7], the characteristic length scale ratio $\bar{h}/h$ for all simulations including a dynamic model is set to 2.5 for the, here exclusively used, scale-separating operator S^{pm}.

At first, the mean streamwise resolved velocity $\langle u_1^h \rangle$ is analyzed. Mean values are obtained by averaging over all time steps of the statistical period as well as over homogeneous x_1–x_3-planes. The mean values are scaled by the wall-shear velocity u_τ, which is calculated for each method at each resolution level, in the respective diagrams. Figs. 1 and 2 depict the results for the lower and higher Reynolds number case, respectively. Due to the second-order accuracy of the underlying numerical method and the relatively coarse discretization, all LES profiles depart considerably from the DNS profile. The differences between the dynamic averaged model with clipping (DAMC) and the present dynamic localization model (DLMC) are relatively small in both cases. There is also hardly any notable difference between using DAMC and DLMC within a multiscale or non-multiscale environment, which confirms observations in [7]. It is emphasized that none of the dynamic modeling approaches provides better results than the ones obtained with no model (NM). This is in accordance with results in [18,28], where a second-order accurate numerical method was used for simulations with the DAMC and, among other things, compared to no-model calculations. For the mean streamwise velocity profiles, DAMC was more or less clearly outperformed by NM at even higher Reynolds numbers $Re_\tau \approx 1000$ and $Re_\tau \approx 1800$ than the ones investigated in the present study. Notable deviations of the profiles from the respective DNS profiles due to the use of a second-order accurate method, combined with a relatively coarse resolution, were also observed in [30] for flows at the same Reynolds numbers used in the present work. All those observations, including the ones made in this study, raise doubts about the usefulness of any dynamic subgrid-scale modeling approach of this form within a second-order accurate numerical method.
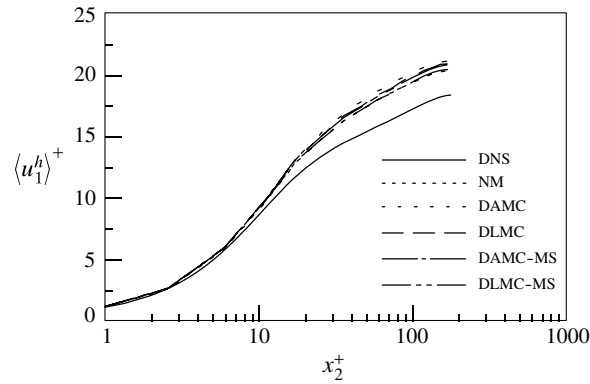
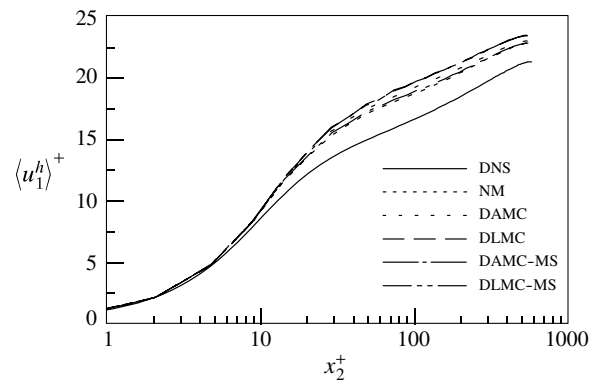Fig. 1. Mean streamwise velocity at $Re_\tau = 180$.

Fig. 2. Mean streamwise velocity at $Re_\tau = 590$.

The turbulent kinetic energy of the resolved scales subject to

$$k^h = \frac{1}{2} \left(\langle u_1^h u_1^h + u_2^h u_2^h + u_3^h u_3^h \rangle - \langle u_1^h \rangle \langle u_1^h \rangle - \langle u_2^h \rangle \langle u_2^h \rangle - \langle u_3^h \rangle \langle u_3^h \rangle \right) \tag{40}$$

is investigated in Figs. 3 and 4, respectively. The kinetic energy values are scaled by u_τ^2 in the respective diagrams. As for the mean streamwise resolved velocity, hardly any difference between any of the applied methods can be recognized. The only notable discrepancy is produced by DAMC for the peak of the turbulent kinetic energy in the lower Reynolds number case. This peak is considerably more overpredicted by this method.
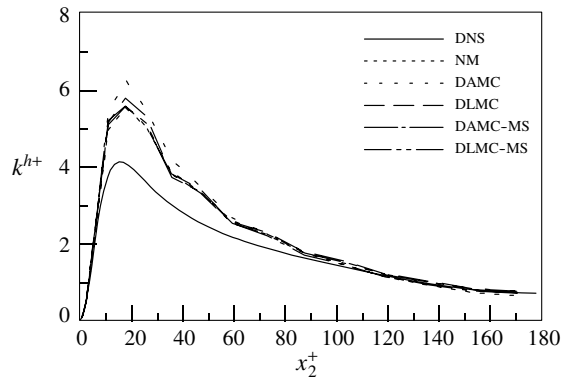

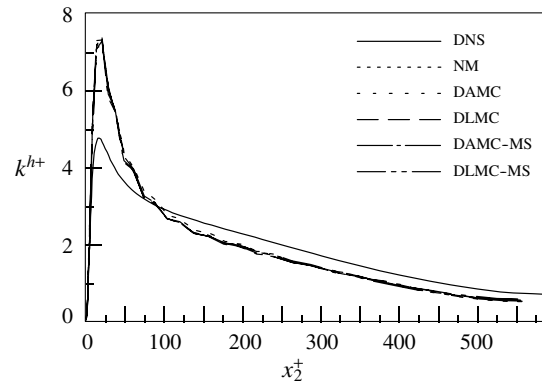Fig. 3. Turbulent kinetic energy at $Re_\tau = 180$.

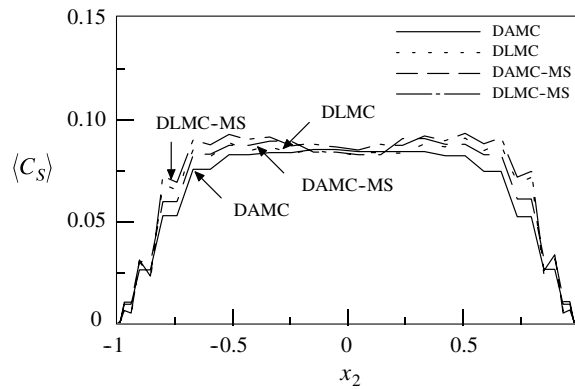Fig. 4. Turbulent kinetic energy at $Re_\tau = 590$.

Fig. 5. Mean value of model parameter C_S at $Re_\tau = 180$.

The mean value of the dynamically determined parameter $\langle C_S \rangle$ is evaluated and compared in Figs. 5 and 6, respectively. The profiles for all methods are similar in the lower Reynolds number case, see Fig. 5. For both DAMC and DLMC, the application within a multiscale environment produces slightly higher values, again confirming observations in [7]. Furthermore, higher values are obtained for DLMC in comparison to DAMC. For the higher Reynolds number case, the profiles appear to be slightly different, see Fig. 6. Notable peaks emerge relatively close to the walls for DLMC.
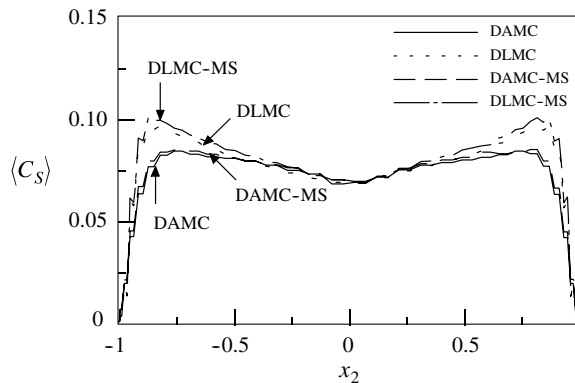

Fig. 6. Mean value of model parameter C_S at $Re_\tau = 590$.

In Figs. 7 and 8, the profiles for the root-mean-square value C_S^{rms} of the dynamically determined parameter C_S are shown. Significant discrepancies between DAMC and DLMC can be observed. With C_S^{rms} almost being negligible for DAMC, very high values overall including distinct peaks are obtained with DLMC. This confirms that a rapidly varying function C_S is indeed produced by the dynamic localization model, which is consistent with the original intention for introducing this model in [6]. In Tables 1 and 2, the picture is quantified for both cases, respectively, by determining volume-averaged mean and root-mean-square values for C_S over the entire domain. The mean values are very close for all methods in both cases. However, substantially higher root-mean-square values are yielded by DLMC compared to DAMC. The root-mean-square values are about 15% and 5% in the lower and higher Reynolds number case, respectively, of the mean value for DAMC. For DLMC, these ratios exceed 300% in both cases (i.e., the standard deviation amounts to more than three times the mean value).

In the second part of the channel flow study, the influence of the discretization level is investigated. The application of DAMC and DLMC within the multiscale environment will be considered no further in this part or in the subsequent diffuser study. This is due to the fact that, consistent with the results in [7], only minor
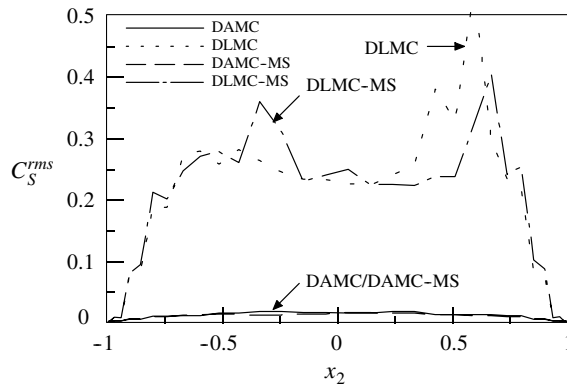

Fig. 7. Root-mean-square value of model parameter C_S at $Re_\tau = 180$.
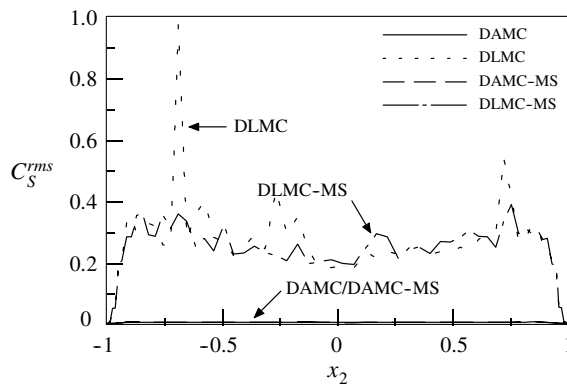
Fig. 8. Root-mean-square value of model parameter C_S at $Re_\tau = 590$.

Table 1
Volume-averaged mean and root-mean-square values of model parameter C_S at $Re_\tau = 180$

	(1): Mean value	(2): Rms value	(3) = (2)/(1) [%]
DAMC	0.067	0.011	16.85
DAMC-MS	0.071	0.010	14.21
DLMC	0.071	0.231	324.52
DLMC-MS	0.074	0.224	302.07

Table 2
Volume-averaged mean and root-mean-square values of model parameter C_S at $Re_\tau = 590$

	(1): Mean value	(2): Rms value	(3) = (2)/(1) [%]
DAMC	0.073	0.004	5.64
DAMC-MS	0.073	0.004	6.06
DLMC	0.077	0.272	352.90
DLMC-MS	0.079	0.252	317.71

differences can be observed in comparison to the non-multiscale application. It is referred to [7] for elaboration of the comparative investigation of subgrid-scale modeling approaches within multiscale and non-multiscale methods. Furthermore, the grid refinement study is restricted to the higher Reynolds number case with $Re_\tau = 590$. Fig. 9 shows the mean streamwise resolved velocity for this case using 4 different discretization levels. By comparing Fig. 9(a) and (b), it is observed that both DAMC and DLMC yield approximately the same convergence to the DNS profile for the two coarser discretizations. For the two finer discretizations, however, in particular the one with 80 control volumes in each coordinate direction, DAMC provides a prediction of the velocity profile which is notably closer to the DNS profile than the one for DLMC.

In Fig. 10, the effect of the discretization level on the turbulent kinetic energy is analyzed. Here, DLMC provides a better prediction for the coarsest discretization. Towards the finer discretization, however, the picture changes again in favor of DAMC. Nevertheless, both methods produce approximately the same results for the turbulent kinetic energy profile on the finest discretization, which is in contrast to the mean streamwise velocity, where DAMC provided better results on this discretization level. In conclusion of all results obtained from the numerical simulations of turbulent flow in a channel, it is stated that DLMC overall produces results comparable but not superior to DAMC.

The grid refinement effect on the mean value $\langle C_S \rangle$ of the model parameter is shown in Fig. 11. It may be observed that refining the discretization even influences the structure of the profile slightly in the central section of the channel for DAMC. Only for the two coarser discretizations, a distinct valley in the profile appears towards the channel center. This valley vanishes for the two finer discretizations. For DLMC, the profiles are shifted almost in parallel in the central section of the channel. For both methods, the peak values decrease and move towards the walls as the discretization becomes finer. For DAMC, this is consistent with observations in [23].

The profiles for the root-mean-square value C_S^{rms} are illustrated in Fig. 12. Whereas the profiles for DAMC are almost invisible in this depiction, hardly any influence of the grid refinement can be observed for DLMC. An excessive peak emerges close to the lower wall for the coarsest discretization as well as a considerably smaller one close to the upper wall. Considerably smaller peaks, which also move towards
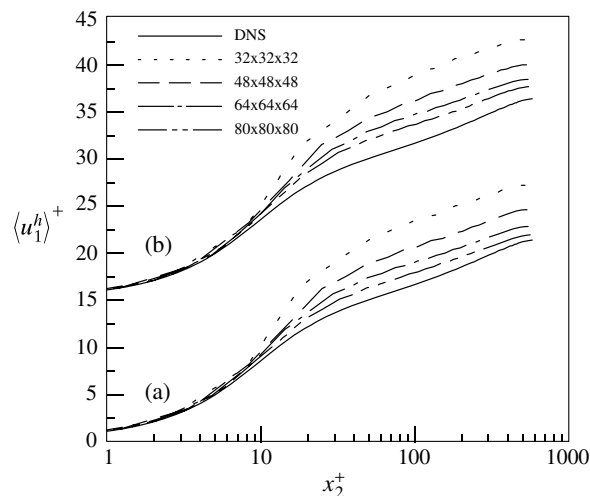

Fig. 9. Grid refinement effect on mean streamwise velocity at $Re_\tau = 590$: (a) DAMC; (b) DLMC (+15).
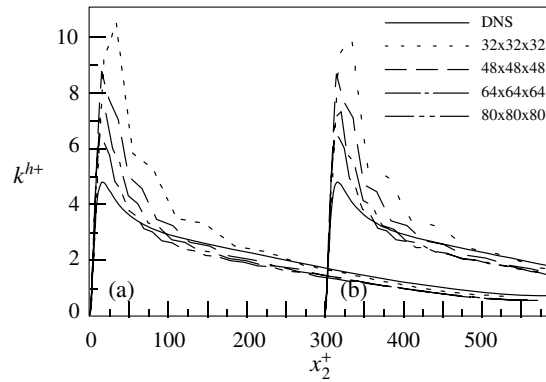
Fig. 10. Grid refinement effect on turbulent kinetic energy at $Re_\tau = 590$: (a) DAMC; (b) DLMC (+300).
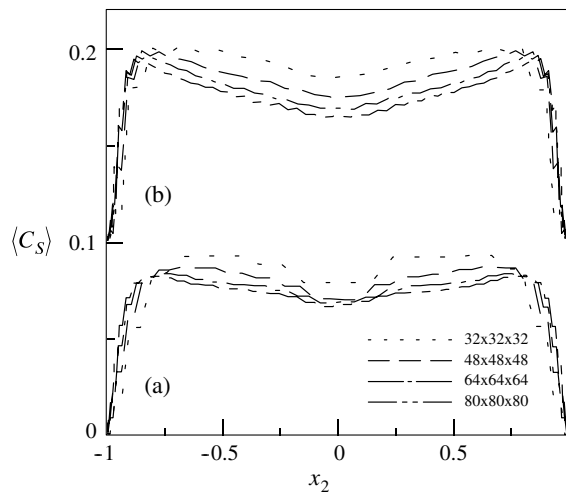
Fig. 11. Grid refinement effect on mean value of model parameter C_S at $Re_\tau = 590$: (a) DAMC; (b) DLMC (+0.1).
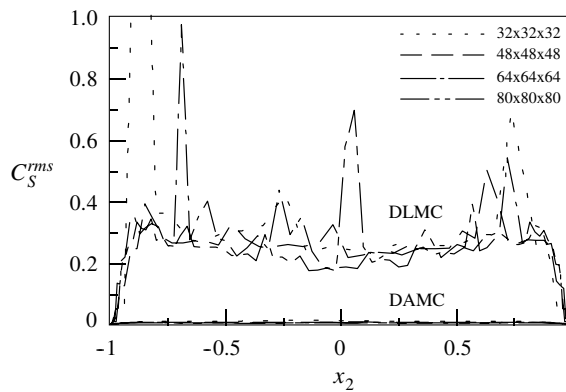
Fig. 12. Grid refinement effect on root-mean-square value of model parameter C_S at $Re_\tau = 590$.

to the channel center, emerge for the discretizations employing 64 and 80 control volumes in each coordinate direction. Surprisingly, however, no such distinct peak can be recognized for the discretization with 48 control volumes in each direction. The quantitative picture is provided in Tables 3 and 4, respectively. The

Table 3
Volume-averaged mean and root-mean-square values of model parameter C_S and clipping percentage at $Re_\tau = 590$: DAMC on various discretizations

|	(1): Mean value	(2): Rms value	(3)=(2)/(1) [%]	(4): Clipped cv [%]
$32 \times 32 \times 32$	0.078	0.009	11.12	12.49
$48 \times 48 \times 48$	0.075	0.006	7.67	7.59
$64 \times 64 \times 64$	0.073	0.004	5.64	2.06
$80 \times 80 \times 80$	0.066	0.003	4.92	0.00

Table 4
Volume-averaged mean and root-mean-square values of model parameter C_S and clipping percentage at $Re_\tau = 590$: DLMC on various discretizations

	(1): Mean value	(2): Rms value	(3) = (2)/(1) [%]	(4): Clipped cv [%]
$32 \times 32 \times 32$	0.086	0.342	398.02	47.70
$48 \times 48 \times 48$	0.081	0.259	319.49	46.89
$64 \times 64 \times 64$	0.077	0.272	352.90	45.93
$80 \times 80 \times 80$	0.068	0.231	341.46	44.92

mean values, the root-mean-values as well as the ratio of these two values are decreasing for both methods when the discretization level increases, with the only exception being the case with 48 control volumes for DLMC. In column (4) of both tables, the statistics of the clipping procedure (i.e., the ad hoc measure common to both methods) are given. It is obvious that, after averaging in the case of DAMC, few control volumes have to be clipped. This clipping percentage ranges from about 12.5% of all control volumes for the coarsest discretization to no clipping at all for the finest discretization. For DLMC, there is substantial need for clipping. Between 45% and 48% of all control volumes are clipped in the investigated cases, with only a slight decrease in the number of clipped control volumes for the finer discretizations.

4.2. Turbulent flow in a diffuser

The numerical setup for turbulent flow in a planar asymmetric diffuser is identical to the one in [9], which is also described in [8]. The diffuser geometry, which basically matches the experimental configuration of [1,25] as well as the numerical setup in [15,32], is shown in Fig. 13. The inlet plane is located at $x_1 = -5$ followed by an inlet channel of length $5\delta_c$, where the inlet channel half-width δ_c, which matches the half-width of the preceding inflow channel, is set to be of unit length. The asymmetric diffuser of length $42\delta_c$ opens with an angle of $10°$. This corresponds to an expansion ratio of $h_{in}/h_{out} = 4.7$. It is followed by an outlet channel of height $9.4\delta_c$

Fig. 13. Diffuser geometry in x_1-x_2-plane.

and length of approximately $58\delta_c$, which locates the outlet plane at about $x_1 = 100$. The outlet channel length matches the one in [32] and is considerably longer than the one in [15]. Due to the relatively long distance between the last point of measurement and the outlet plane, any significant upstream influence of the outlet plane is minimized. Nevertheless, the recovery into a canonical channel flow will not be reached even within this longer outlet channel, see [1,15]. Both the upstream corner at $x_1 = 0$ and the downstream corner at $x_1 = 42$ are rounded with a radius of $r = 19.4$, where the curvature centers are located as shown in Fig. 13. The length of the domain in x_3-direction (i.e., orthogonal to the depiction in Fig. 13) is chosen to be $8\delta_c$ matching the spanwise length in [32] and representing the largest value for the spanwise length investigated in [15]. The inflow channel matches the inlet channel in its dimensions in x_2- and x_3-direction. According to [32], an inflow channel length of $12\delta_c$ is chosen.

A zero velocity field is assumed to be the initial condition for the velocity. At the walls Γ_w, no-slip boundary conditions (i.e., $\boldsymbol{g} = 0$ in (4)) are assumed throughout the simulation time T. At the inflow boundary Γ_{in}, a time-dependent inflow velocity vector $\boldsymbol{g} = \boldsymbol{u}^{in}(t)$ is prescribed. The inflow velocity $\boldsymbol{u}^{in}(t)$ is generated in the inflow channel as a result of a fully developed turbulent flow. At the outflow boundary Γ_{out}, a convective boundary condition is prescribed subject to

$$\frac{\partial \boldsymbol{u}}{\partial t} + u^{out} \frac{\partial \boldsymbol{u}}{\partial x_1} = 0 \quad \text{on } \Gamma_{out} \times (0, T), \tag{41}$$

where u^{out} is calculated such that overall conservation is maintained (i.e., the mass flux through the outflow boundary equals the mass flux through the inflow boundary). Finally, periodic boundary conditions are assumed on the boundaries Γ_{per} in x_3-direction (i.e., this periodicity is assumed orthogonal to the depiction in Fig. 13).

Flow at Reynolds number $Re_\tau = u_\tau \delta_c / v = 500$ is simulated in the inflow channel, where u_τ denotes the turbulent wall-shear velocity. The velocity at the outlet plane of the inflow channel represents the inflow velocity $\boldsymbol{u}^{in}$ for the diffuser. The Reynolds number for the flow in the diffuser is determined based on the streamwise bulk mean velocity u_b (i.e. $Re_b = u_b \delta_c / v$). The corresponding Reynolds numbers Re_b range from about 10,800 to 11,200 and are, thus, slightly higher than 9,000, which is the approximate Reynolds number in the aforementioned experimental and numerical studies. However, the flow appears to be insensitive to the Reynolds number in this higher Reynolds number range according to [15].

The inflow channel is spatially discretized using $80 \times 64 \times 80$ control volumes in x_1-, x_2-, and x_3-direction, respectively. The distribution of control volumes in the wall-normal direction obeys a cosine function refining towards the walls for the parent grid, with the subsequent hierarchical subdivision procedure applied. Compared to the discretization of the inflow channel in [32], which employed 128 control volumes in each coordinate direction, less than 20% the number of control volumes are used in the present case. The actual diffuser including inlet and outlet channel is discretized using $290 \times 64 \times 80$ control volumes in x_1-, x_2-, and x_3-direction, respectively. The control volumes are uniformly distributed in the spanwise direction as in the inflow channel. In the wall-normal direction, the same cosine function for refinement towards the walls is used as in the inflow channel. This leads to an equivalent distribution in the inlet channel, which is then spread in the asymmetric part of the diffuser. In the streamwise direction, the following control volume distribution is employed: In the inlet channel, h_1 decreases linearly from 0.15 to 0.05, in the asymmetric diffuser part, h_1 increases linearly from 0.05 to 0.475, in the first part of the outlet channel (ranging from $x_1 = 42$ to $x_1 = 74.5$), h_1 increases linearly from 0.475 to 0.825, and in the remaining part of the outlet channel, the control volumes are uniformly distributed with $h_1 = 0.825$. Comparing the discretization of the diffuser to the finer discretization in [32], which employed $590 \times 100 \times 110$ control volumes in x_1-, x_2-, and x_3-direction, it is stated that less than 23% the number of control volumes are used in the present case.

Both for the inflow channel and the diffuser simulation, the time step δt is fixed to be 0.002. 5,000 time steps are performed to allow the flow to develop, and the statistics as well as the inflow velocity data are collected during another 10,000 time steps. As a consequence, inflow data for 20 time units are available, which represents a sufficient period for a fluid particle to be converted over a distance roughly equal to the streamwise diffuser dimension including inlet and outlet channel. In the actual diffuser simulation, 40,000 time steps corresponding to 80 time units are performed to allow the flow to develop, and the statistics are collected during another 40,000 time steps. Thus, the inflow data are recycled 8 times during the diffuser simulation. As in the

previous example, the characteristic length scale ratio $\bar{h}/h$ for all simulations including a dynamic model is set to 2.5 for the scale-separating operator S^{pm}.

In the diffuser, the mean streamwise resolved velocity $\langle u_1^h \rangle$ is evaluated as profiles in the wall-normal direction x_2 at four different locations in streamwise direction. These locations are distributed along the diffuser as follows: one behind the entry to the asymmetric diffuser section ($x_1 = 6.4$), one in the middle ($x_1 = 22.4$), one close to the end ($x_1 = 38.4$), and one in the outlet channel ($x_1 = 58.4$). These locations correspond to locations where experimental as well as numerical results are available from the studies in [25,32]. At the same locations, the root-mean-square values for the streamwise and wall-normal resolved velocities $u_1^{h,\text{rms}}$ and $u_1^{h,\text{rms}}$ are evaluated. All mean and root-mean-square values in the diffuser are obtained by averaging over all time steps of the statistical period as well as over the homogeneous x_3-direction. Both mean and root-mean-square velocities are scaled by the streamwise bulk mean velocity u_b. The velocity results are compared to the numerical data from [32], hereafter referred to as "Wu-LES", and to the experimental data from [25], hereafter referred to as "Obi-experiment".

Fig. 14 depicts the profiles for the mean streamwise resolved velocity at these locations. Overall, it may be observed that, on the one hand, the profiles for the dynamic model with special clipping (DMSC) and the present dynamic localization model (DLMC) are almost indistinguishable and, on the other hand, also fairly close to the reference data, in particular the numerical reference data from the Wu-LES. From the middle of the asymmetric diffuser section on, the numerical data exhibit slight deviations from the experimental data, in particular towards the upper wall. The effect of the model can immediately be recognized by comparing the two methods with a dynamic model to NM (i.e., the data obtained with no model at all).

Similar observations may generally be made for the streamwise root-mean-square values of the velocity at the first two locations in Figs. 15(a) and (b), although both DMSC and DLMC exhibit a notable deviation from the numerical and experimental reference data closer to the walls in Fig. 15(a). Further downstream in the diffuser, the deviations from the reference data become more distinct, and slight discrepancies between the two dynamic models emerge as well, without, however, showing a clear advantage for one or the other model, see Figs. 15(c) and (d). The situation looks similar for the wall-normal root-mean-square values of the velocity in Fig. 16. However, particularly towards the end of the asymmetric diffuser section and in the outlet channel, slightly better results are obtained with DLMC than with DMSC, see Figs. 16(c) and (d).

Both along the upper and lower walls of the diffuser, the wall static pressure coefficient defined as

$$C_{\text{pw}}(x_1) = \frac{\langle p_w^h \rangle(x_1) - \langle p_w^h \rangle(x_1 = -5)}{\frac{1}{2}\rho u_b^2}, \tag{42}$$

where p_w^h denotes the discrete pressure value at the walls, and the skin friction coefficient subject to
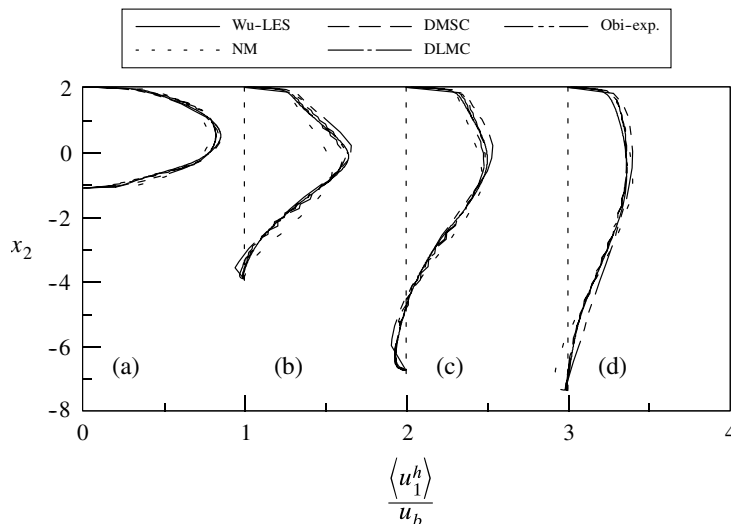

Fig. 14. Mean streamwise velocity: (a) $x_1 = 6.4$; (b) $x_1 = 22.4$ (+1); (c) $x_1 = 38.4$ (+2); (d) $x_1 = 58.4$ (+3).
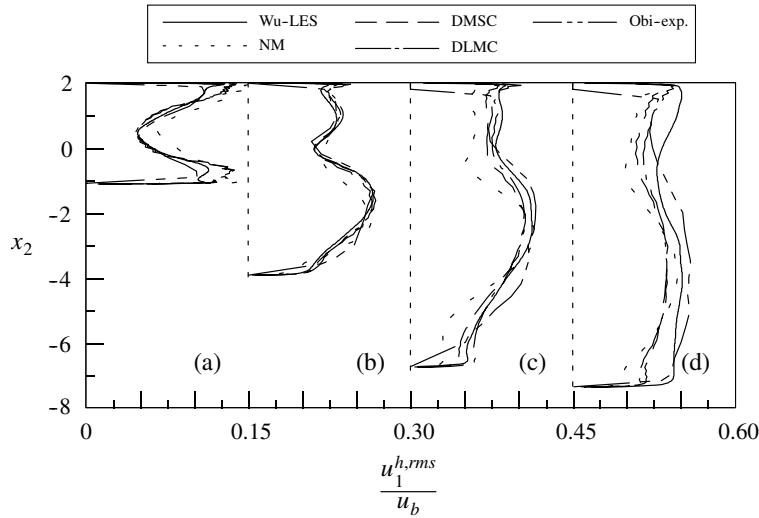
Fig. 15. Rms streamwise velocity: (a) $x_1 = 6.4$; (b) $x_1 = 22.4$ (+0.15); (c) $x_1 = 38.4$ (+0.30); (d) $x_1 = 58.4$ (+0.45).
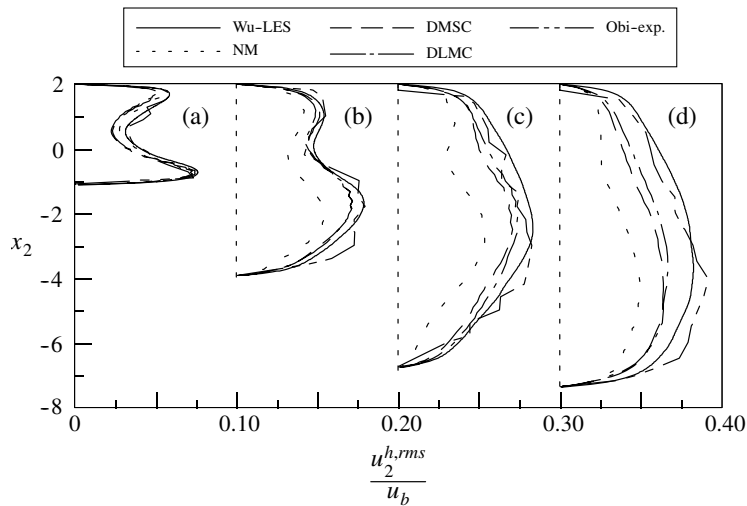

Fig. 16. Rms wall-normal velocity: (a) $x_1 = 6.4$; (b) $x_1 = 22.4$ (+0.10); (c) $x_1 = 38.4$ (+0.20); (d) $x_1 = 58.4$ (+0.30).

$$C_f(x_1) = \frac{\langle \tau_w^h \rangle (x_1)}{\frac{1}{2} \rho u_b^2}, \tag{43}$$

where τ_w^h denotes the discrete value of the wall shear stress, are evaluated as functions of the streamwise direction x_1, respectively. In both (42) and (43), the fluid density ρ is assumed to be of unit value. The results for the two coefficients in (42) and (43) are compared to the numerical data from the Wu-LES. Furthermore, the results for the skin friction coefficient are compared to the experimental data from Buice and Eaton [1], hereafter referred to as "Buice-experiment". Due to the fact that the reference pressure value was chosen at a different location in the Buice-experiment, namely $x_1 = -3.4$ for the present configuration, it is not possible to accurately compare the results for the wall static pressure coefficient as well.

In Figs. 17 and 18, the profiles of the wall static pressure coefficient along the upper and lower walls are shown, respectively. It is noted that both DLMC and DMSC are closer to the reference data than NM, and that DLMC gives even a slightly better prediction. Figs. 19 and 20 depict the skin friction coefficient along the upper and lower wall, respectively. Both along the upper and lower wall, DLMC and DMSC are almost
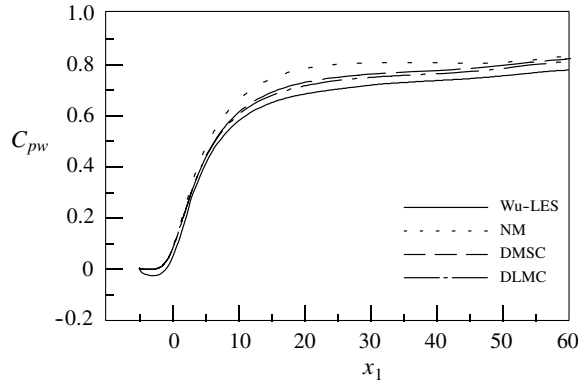
Fig. 17. Wall static pressure coefficient along the upper wall of the diffuser.
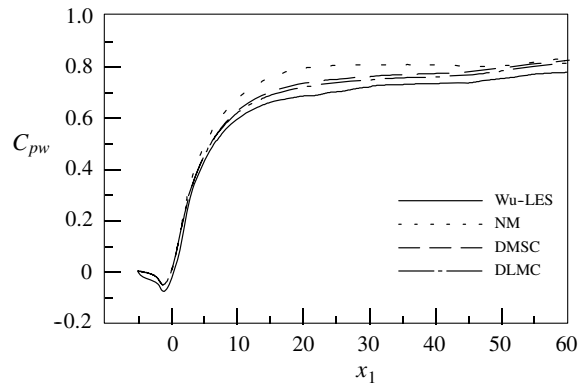

Fig. 18. Wall static pressure coefficient along the lower wall of the diffuser.
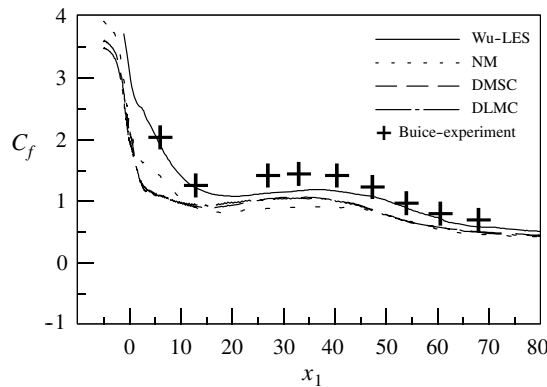

Fig. 19. Skin friction coefficient (factor 1000) along the upper wall of the diffuser.

indistinguishable, with the only exception being the section between $x_1 \approx 2$ and $x_1 \approx 15$ at the lower wall, where DMSC performs slightly better than DLMC. Nevertheless, both methods provide a worse prediction than NM in most of this section along both the upper and lower wall. Further downstream, however, the situation is reversed.

The mean value of the model parameter $\langle C_S \rangle$ is evaluated at the four locations specified above in Fig. 21. It is obvious that the values obtained with DMSC are considerably larger than the ones obtained with DLMC. This is likely the result of the different clipping procedure used in these two models. Due to the fact that
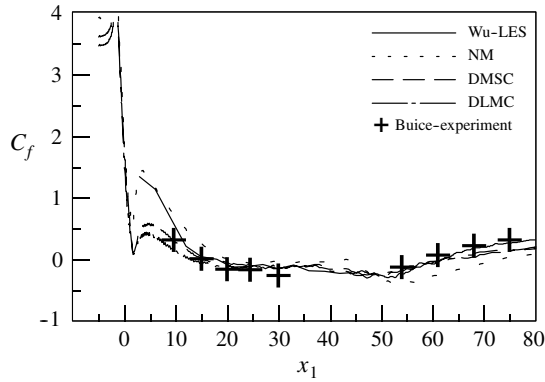
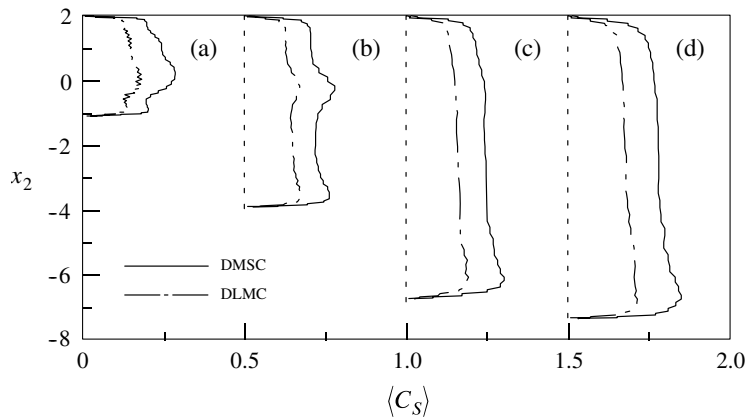Fig. 20. Skin friction coefficient (factor 1000) along the lower wall of the diffuser.

Fig. 21. Mean value of model param. C_S: (a) $x_1 = 6.4$; (b) $x_1 = 22.4$ (+0.5); (c) $x_1 = 38.4$ (+1.0); (d) $x_1 = 58.4$ (+1.5).

DMSC always produces a positive value and DLMC is supposed to be zero in a clipped control volume, it should be expected that the mean value is larger for DMSC overall. Aside from the actual value, both DMSC and DLMC produce qualitatively very similar profiles as confirmed in Fig. 21.

The profiles for the root-mean-square value C_S^{rms} are investigated in Fig. 22. Large values with distinct peaks emerge for DLMC at each location, as in the channel flow. However, the root-mean-square values for DMSC are definitely not negligible in contrast to the ones for DAMC in the channel. This is obviously
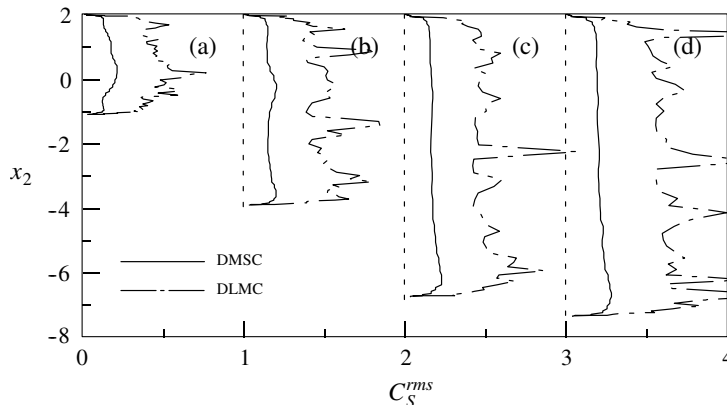

Fig. 22. Rms value of model parameter C_S: (a) $x_1 = 6.4$; (b) $x_1 = 22.4$ (+1); (c) $x_1 = 38.4$ (+2); (d) $x_1 = 58.4$ (+3).

Table 5
Volume-averaged mean and root-mean-square values of model parameter C_S in the inflow channel

	(1): Mean value	(2): Rms value	(3) = (2)/(1) [%]
DAMC	0.070	0.006	9.10
DMSC	0.160	0.106	66.45
DLMC	0.097	0.322	332.92

Table 6
Mean and root-mean-square values of model parameter C_S and clipping percentage in the diffuser (mean and root-mean-square values are obtained as an average of the results at the four investigated locations along the diffuser)

	(1): Mean value	(2): Rms value	(3) = (2)/(1) [%]	(4): Clipped cv [%]
DMSC	0.243	0.179	73.39	37.13
DLMC	0.155	0.509	328.17	46.99

due to the fact that no averaging at all is performed. The quantitative picture is provided in Tables 5 and 6. Firstly, the results from the independently simulated turbulent inflow channel are given in Table 5. These data provide an opportunity to compare all three methods, DAMC, DMSC, and DLMC. The mean value for DMSC is substantially larger than the one for the other methods, which are roughly comparable. In terms of the root-mean-square value and the ratio of the mean value and the root-mean-square value, a clear order may be observed with DLMC producing the largest value, DMSC a medium value, and DAMC the smallest value. As in the channel flow, the standard deviation amounts to more than three times the mean value for DLMC. For DMSC, the standard deviation is of the same order of magnitude as the mean value. For DAMC, it is approximately ten times (i.e., about one order of magnitude) smaller than the mean value. The numbers for DMSC and DLMC are confirmed in the actual diffuser, see Table 6. The data in columns (l)–(3) of Table 6 are calculated as an average over the four locations specified above. In column (4) of Table 6, the clipping percentage for the *complete* diffuser domain is given. About 10% less control volumes are clipped for DMSC than for DLMC. The clipping percentage for DLMC in the diffuser is also similar to the one in the channel.

Finally, a remark should be made concerning an important implication of the rapidly varying function C_S. In both channel and diffuser applications, a very slow convergence has been observed for the SOR solver in the solution procedure of the matrix resulting from the discretization of the momentum equation. This may directly be ascribed to the influence of this highly fluctuating function within the momentum equation, since this slow convergence has not been observed for any of the other methods applied in this study. Thus, a more efficient solver should be used in future applications of the dynamic localization model to reduce the excessive time spent in the solution of the momentum equation. It is pointed out that this results from the use of the dynamic localization model in general and is not exclusively related to the present implementation of the model.

5. Conclusions

A new approach for a dynamic localization model has been proposed in this work. This approach has been consistently integrated into LES based on a variational formulation, since the variationally formulated condition for the model parameter has been considered as an additional equation in a resulting system of two variational equations. This variational system may be solved either using a finite element or a finite volume method. The new version of the dynamic localization proposed in this work has three important advantages compared to the original dynamic localization model in [6].

- The solution of the new dynamic localization model is based on a simpler formulation, since the variationally formulated condition for the model parameter is actually solved as a variational equation. This obviates the need to use a rather complicated Fredholm integral equation of the second kind for its solution as proposed in [6].
- The solution of the integral equation as proposed in [6] had to be done iteratively. This is not necessary for the new approach, since it may simply be solved as a linear variational equation.

- A number of small independent local equations equal to the number of parent elements or control volumes can be solved instead of one large global equation in [6]. Thus, the actual solution procedure may be executed completely in parallel in a multi-processor simulation, in contrast to required inter-processor communications during the solution of a global equation.

Moreover, it should be emphasized that no approximation as in [26] and no exploitation of any homogeneous coordinate directions as in [31] has been necessary in the development of this new approach. The only ad hoc measure remaining in the present approach is a clipping procedure for elements or control volumes exhibiting negative values of C_S. The clipping is done to prevent potential instabilities in the course of the simulation. However, a similar measure had to be taken for the dynamic localization model (constrained) in [6]. A few hints for a potential extension of the consistent dynamic localization model (constrained) to a consistent dynamic localization model (k-equation) based on the one proposed in [6] have been given at the end of Section 3.

The new consistent dynamic localization model has been tested for two different numerical flow examples, turbulent flow in a channel and turbulent flow in a planar asymmetric diffuser. For the channel flow simulations, it has been compared to the original dynamic model according to [5] with averaging over the homogeneous planes of the channel. Results of similar quality have been achieved for both modeling procedures, with, however, the original dynamic model providing slightly better results for finer discretizations, and the dynamic localization model giving slightly better predictions for coarser discretizations. Furthermore, no significant differences have been observed between using the dynamic models either in a multiscale or a non-multiscale environment, which is consistent with observations in [7]. Although the profiles for the mean value of the model parameter have been similar, significant differences have been observed for the root-mean-square value of the model parameter exhibiting very large values for the dynamic localization model. This indicates that using the dynamic localization model indeed produces a rapidly varying model parameter function consistent with observations in [22]. In the end, however, allowing for those rapid variations of the model parameter function in the dynamic localization model does not produce superior results compared to the original dynamic model with averaging over the homogeneous planes, where the rapid variations are not taken into account. For the diffuser flow simulations, the dynamic localization model has been compared to the dynamic model with special clipping according to [20]. Here again, the results are of similar quality with slightly better results for the dynamic localization model, in particular for the wall static pressure coefficient and the root-mean-square velocities in the wall-normal direction towards the end of the asymmetric diffuser section and in the outlet channel. It has been confirmed for this example as well that the model parameter function is a rapidly varying function when using the dynamic localization model. A furthergoing physical analysis of those rapid variations appears to be necessary. A beneficial effect on the numerical results by taking into account the rapid variations has indeed not been proven for both numerical examples. However, it has also been found that, in order to deal with such highly fluctuating functions in a computationally efficient manner, more sophisticated solvers should be used to reduce computational cost.

For the relatively simpler numerical flow examples in the present study (i.e. flow situations with at least one homogeneous flow direction), the use of the dynamic localization model instead of the slightly more inconsistent classical dynamic model or the dynamic model with special clipping, respectively, does not appear to be advisable. This is due to the still higher complexity of the dynamic localization model, although it has already been substantially reduced with respect to the original model version in [6]. However, as already cited from the original study in [5] in the introduction, the development of the dynamic localization model aimed at "putting the dynamic modeling procedure on firm theoretical foundations, so that the method could be applied to arbitrary inhomogeneous flows without recourse to ad hoc procedures". As a result, this model particularly aims at completely inhomogeneous flows. In such flows, there is, on the one hand, no homogeneous spatial direction at all, such that approaches like the spatially averaged classical dynamic model are useless, and, on the other hand, the use of other ad hoc procedures, such as the special clipping, might also not be justified. The dynamic localization model represents a consistent approach for any arbitrary inhomogeneous flow. Furthermore, it has also proven to produce, at least, no worse results than dynamic models with ad hoc procedures for the simpler numerical flow situations considered here (i.e., turbulent channel and diffuser flow) and in [6] (i.e., isotropic turbulence and turbulent flow over a backward-facing step). It is hoped that the advantages of the

new version of the dynamic localization model proposed in the present study, which substantially reduce the required computational effort, might encourage researchers to use the dynamic localization model for arbitrary inhomogeneous flows.

Acknowledgments

References

[1] C.U. Buice, J.K. Eaton, Experimental investigation of flow through an asymmetric plane diffuser, Report TSD-107, Department of Mechanical Engineering, Stanford University, 1997.

[2] D. Carati, S. Ghosal, P. Moin, On the representation of backscatter in dynamic localization models, Phys. Fluids 7 (3) (1995) 606–616.

[3] T. Dubois, F. Jauberteau, R. Temam, Dynamic Multilevel Methods and the Numerical Simulation of Turbulence, Cambridge University Press, Cambridge, 1999.

[4] M. Germano, Turbulence: the filtering approach, J. Fluid Mech. 238 (1992) 325–336.

[5] M. Germano, U. Piomelli, P. Moin, W.H. Cabot, A dynamic subgrid-scale eddy viscosity model, Phys. Fluids A 3 (7) (1991) 1760–1765.

[6] S. Ghosal, T.S. Lund, P. Moin, K. Akselvoll, A dynamic localization model for large-eddy simulation of turbulent flows, J. Fluid Mech. 286 (1995) 229–255.

[7] V. Gravemeier, Scale-separating operators for variational multiscale large eddy simulation of turbulent flows, J. Comput. Phys. 212 (2006) 400–435.

[8] V. Gravemeier, The variational multiscale method for laminar and turbulent flow, Arch. Comput. Meth. Eng., in press.

[9] V. Gravemeier, Variational multiscale large eddy simulation of turbulent flow in a diffuser, Comput. Mech., in press.

[10] V. Gravemeier, W.A. Wall, E. Ramm, Large eddy simulation of turbulent incompressible flows by a three-level finite element method, Int. J. Numer. Meth. Fluids 48 (2005) 1067–1099.

[11] F. Ham, S. Apte, G. Iaccarino, X. Wu, M. Herrmann, G. Constantinescu, K. Mahesh, P. Moin, Unstructured LES of reacting multiphase flows in realistic gas turbine combustors, in: Annual Research Briefs – 2003, Center for Turbulence Research, Stanford University and NASA Ames Research Center, 2003, pp. 139–160.

[12] T.J.R. Hughes, L. Mazzei, K.E. Jansen, Large eddy simulation and the variational multiscale method, Comput. Visual. Sci. 3 (2000) 47–59.

[13] T.J.R. Hughes, L. Mazzei, A.A. Oberai, A.A. Wray, The multiscale formulation of large eddy simulation: decay of homogeneous isotropic turbulence, Phys. Fluids 13 (2) (2001) 505–512.

[14] T.J.R. Hughes, A.A. Oberai, L. Mazzei, Large eddy simulation of turbulent channel flows by the variational multiscale method, Phys. Fluids 13 (6) (2001) 1784–1799.

[15] H.-J. Kaltenbach, M. Fatica, R. Mittal, T.S. Lund, P. Moin, Study of flow in a planar asymmetric diffuser using large-eddy simulation, J. Fluid Mech. 390 (1999) 151–185.

[16] D. Kim, H. Choi, A second-order time-accurate finite volume method for unsteady incompressible flow on hybrid unstructured grids, J. Comput. Phys. 162 (2000) 411–428.

[17] B. Koobus, C. Farhat, A variational multiscale method for the large eddy simulation of compressible turbulent flows on unstructured meshes – application to vortex shedding, Comput. Meth. Appl. Mech. Eng. 193 (2004) 1367–1383.

[18] A.G. Kravchenko, P. Moin, On the effect of numerical errors in large eddy simulations of turbulent flows, J. Comput. Phys. 131 (1997) 310–322.

[19] D.K. Lilly, A proposed modification of the Germano subgrid-scale closure method, Phys. Fluids A 4 (3) (1992) 633–635.

[20] K. Mahesh, G. Constantinescu, S. Apte, G. Iaccarino, F. Ham, P. Moin, Progress toward large-eddy simulation of turbulent reacting and non-reacting flows in complex geometries, in: Annual Research Briefs – 2002, Center for Turbulence Research, Stanford University and NASA Ames Research Center, 2002, pp. 115–142.

[21] K. Mahesh, G. Constantinescu, P. Moin, A numerical method for large-eddy simulation in complex geometries, J. Comput. Phys. 197 (2004) 215–240.

[22] P. Moin, A new approach for large eddy simulation of turbulence and scalar transport, in: Proc. Monte Verita Coll. on Turbulence, Birkhäuser, Bale, 1991.

[23] Y. Morinshi, O.V. Vasilyev, Vector level identity for dynamic subgrid scale modeling in large eddy simulation, Phys. Fluids 14 (10) (2002) 3616–3623.

[24] R.D. Moser, J. Kim, N.N. Mansour, Direct numerical simulation of turbulent channel flow up to $Re_\tau = 590$, Phys. Fluids 11 (4) (1999) 943–945.

[25] S. Obi, K. Aoki, S. Masuda, Experimental and computational study of turbulent separating flow in an asymmetric plane diffuser, in: Ninth Symposium on Turbulent Shear Flows, Kyoto, Japan, August 16–19, 1993.

[26] U. Piomelli, J. Liu, Large-eddy simulation of rotating channel flows using a localized dynamic model, Phys. Fluids 7 (4) (1995) 839–848.

[27] P. Sagaut, Large Eddy Simulation for Incompressible Flows, second ed., Springer, Berlin, 2002.

[28] K.B. Shah, J.H. Ferziger, A new non-eddy viscosity subgrid-scale model and its application to channel flow, in: Annual Research Briefs – 1995, Center for Turbulence Research, Stanford University and NASA Ames Research Center, 1995, pp. 73–90.

[29] J. Smagorinsky, General circulation experiments with the primitive equations. I. The basic experiment, Mon. Weather Rev. 91 (1963) 99–164.

[30] M. Terracol, P. Sagaut, C. Basdevant, A multilevel algorithm for large-eddy simulation of turbulent compressible flows, J. Comput. Phys. 167 (2001) 439–474.

[31] B.-C. Wang, P.P. LePoudre, D.J. Bergstrom, A direct solution method for the dynamic localization model for large-eddy simulation of turbulent flows with homogeneous dimensions, Proceedings of the Eleventh Annual Conference of the CFD Society of Canada, Vancouver, BC, May 28–30, 2003, pp. 733–740.

[32] X. Wu, J. Schlüter, P. Moin, H. Pitsch, G. Iaccarino, F. Ham, Computational study on the internal layer in a diffuser, J. Fluid Mech. 550 (2006) 391–412.

[33] Y. Zang, R.L. Street, J.R. Koseff, A dynamic mixed subgrid-scale model and its application to turbulent recirculating flows, Phys. Fluids A 5 (1993) 3186–3196.

[34] O.C. Zienkiewicz, R.L. Taylor, The Finite Element Method, Vol. 1: The Basis, fifth ed., Butterworth-Heinemann, Oxford, 2000.